Supplemental Document

Stress tensor mesostructures for deterministic figuring of thin substrates: supplement

YOUWEI YAO,[1] BRANDON CHALIFOUX,[2] RALF K. HEILMANN,[1] AND MARK L. SCHATTENBURG[1,*]

[1] *Space Nanotechnology Laboratory, MIT Kavli Institute for Astrophysics and Space Research, Massachusetts Institute of Technology, 77 Massachusetts Avenue, Cambridge, Massachusetts 02139, USA*
[2] *James C. Wyant College of Optical Sciences, The University of Arizona, 1630 E. University Blvd., Tucson, Arizona 85721-0094, USA*
[*] *Corresponding author: marks@space.mit.edu*

Supplement DOI: https://doi.org/10.6084/m9.figshare.19294301

Parent Article DOI: https://doi.org/10.1364/OPTICA.445379

Stress tensor mesostructures for deterministic figuring of thin substrates

YOUWEI YAO, BRANDON CHALIFOUX, RALF HEILMANN, AND MARK SCHATTENBURG

Correspondence to: marks@space.mit.edu

Limitation of deformations created by equibiaxial stress fields

Based on a previous study [1], conventional coating stress on flat wafer substrates [2, 3] can only exactly generate a restricted set of Zernike deformations (denoted as Z_{nm} where n is the radial degree and m is the azimuthal order) over the full aperture of a substrate, such as sphere (defocus) (Z_{20}), primary coma (Z_{31} and $Z_{3\text{-}1}$) and 2nd order sphere (Z_{40}), due to the fact that stress fields in conventional coatings are equibiaxial. Fig. S1 illustrates the Zernike polynomial deformations and the corresponding stress fields required to achieve them. For the components in red and yellow and using equibiaxial stress only, approximate correction over a full aperture or exact correction over a sub-aperture are possible, but exact correction over a full aperture is not. For example, the generation of the astigmatism term (Z_{22}) needs an antibiaxial stress with fixed magnitude and orientation (Eq. S1). In addition, the generation of trefoil (Z_{33}) requires antibiaxial stress, but the magnitude and orientation vary with location as demonstrated in Eq. S2.

$$N_1 = S_0, \quad N_2 = -S_0, \quad \phi = 0 \tag{S1}$$

$$N_1 = S_0 \times \frac{r}{R}, \quad N_2 = -S_0 \times \frac{r}{R}, \quad \phi = \frac{1}{2}(\pi - \theta) \tag{S2}$$

Here N_1 and N_2 are the local principal stresses with orientation of coordinate ϕ, S_0 is a constant, and R is the radius of the substrate. The stresses are expressed in polar coordinates where (r, θ) represents the location on the substrate. Fig. S2 shows a sketch of the local stresses in these coordinates.

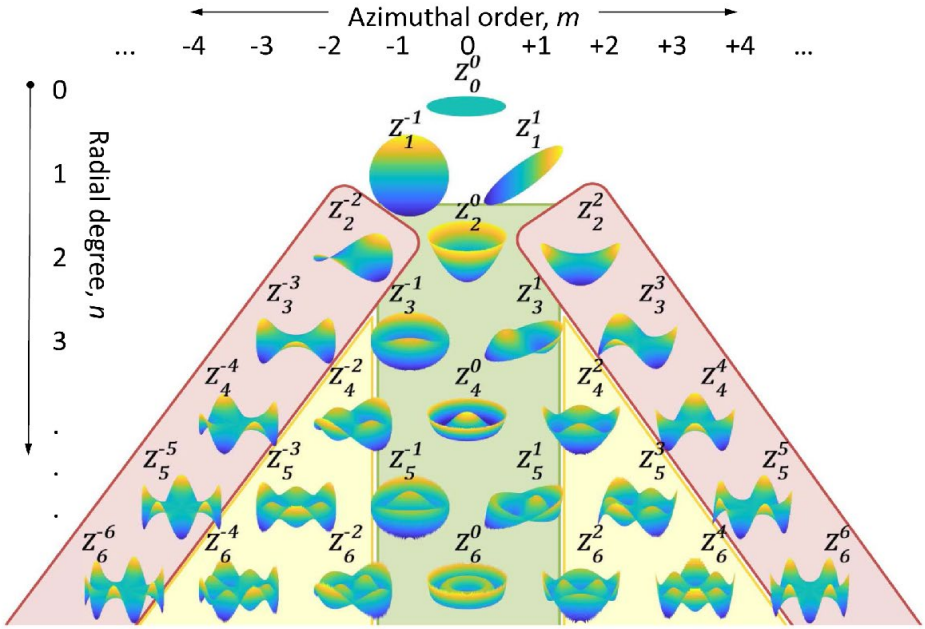

Fig. S1. Different Zernike polynomial zones require different types of stress to achieve deformation (reprinted from ref. 1). The center three columns of deformation (green zone) require equibiaxial stress fields. The pyramid shoulder (red zone) requires antibiaxial stress fields. The intermediate zone (yellow zone) requires a combination of both.

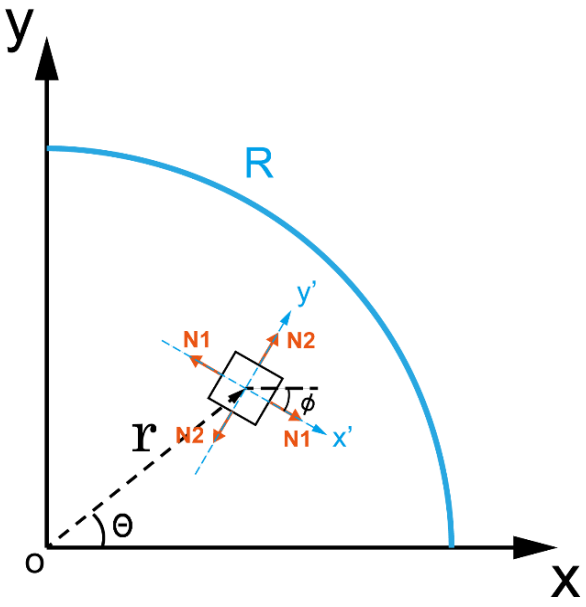

Fig. S2. Sketch of the local principal stresses in polar coordinates. N_1 and N_2 are the principal stresses with orientation of ϕ. x-y and x'-y' indicate global and local Cartesian coordinate systems, respectively. In this work, R is the radius of the silicon wafer.

2D FE modeling of deformations created by trenched lines on coated surfaces

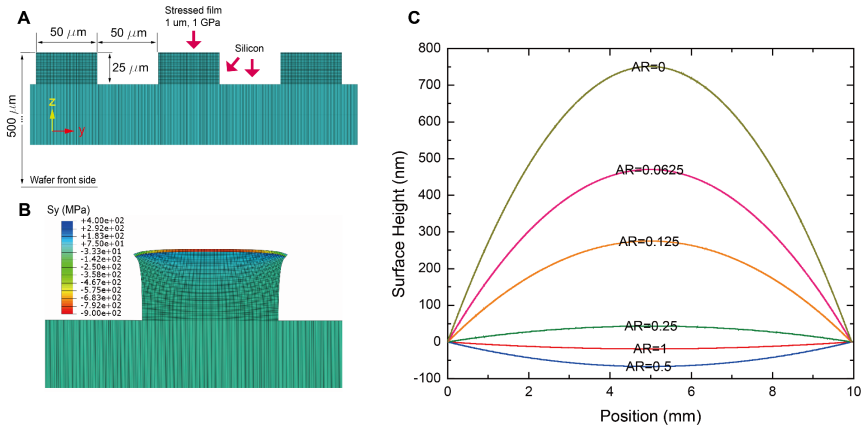

Fig. S3. 2D FE modeling of deformations created by trenched lines on coated surfaces. (a) Sketch of a 2D model showing a cross section of the trenched surface with AR=0.5. (b) Calculated deformation and stress distribution of one tooth of the grating. Note that stress in the y direction is relaxed at the corners. (c) Calculated deformation of wafer front sides for different ARs. (Note 1: Since the thickness of the 2D model is 0.525 mm, which is much less than the length in the y direction (10 mm), the calculated curvature for different ARs (which is the key for deriving the red solid line in Fig. 1(c)) is not affected by the different size in the y direction between the model and real wafers. Note 2: Print-through is not evident in the calculated profiles in (c).)

We developed 2D FE models in Abaqus to analyze the deformation created by trenched lines on coated surfaces. Figs. S3(a) and S3(b) depict the local geometry, deformations and stress distributions of the model with AR=0.5. FE meshes are visible on the plot. There are 898,000 mesh elements in the 2D model with AR=0.5. Each tooth has 50×100 rectangular mesh elements, and the remained area underneath the teeth structure has 20×19,900 rectangular mesh elements. Since the models are two-dimensional, the element type is set as a plane strain for analyzing the cross sections (CPE4I in Abaqus). As for the boundary conditions, the left bottom corner of the model is constrained to be no displacement (U_x=U_y=0), while the right bottom corner has the constraint in vertical direction (U_y=0) which can slide horizontally. Fig. S3(c) shows calculated deformations for different ARs. The curvature of each profile represents the equivalent stress in the fictitious films along the y direction. The normalized stresses are calculated by using the wafer with AR=0 as reference. Results are plotted with a solid red line in Fig. 1(c).

Metrology and repeatability tests

In this work we use a Shack-Hartmann metrology tool [4] to measure the deformation of 100-mm-diameter, 0.525 mm-thick silicon wafers generated by stress patterns. The tool is enclosed in a windshield structure to mitigate the influence of turbulence. The wafer mount is carefully designed to hold the wafer vertically for minimum distortion [5]. A nickel-coated aluminum block with surface flatness of λ/4 is integrated into the wafer mount to serve as a reference surface. The measured raw data is fitted by 36 terms of Zernike polynomials. Fig. S4 shows the result of a repeatability test. A silicon wafer was mounted, measured, and removed from the tool 10 times to test repeatability. In the test, the mean coefficient of each Zernike term is used as a reference. The first three terms are omitted since they represent offset, tip and tilt, which have no impact on the measured profile.

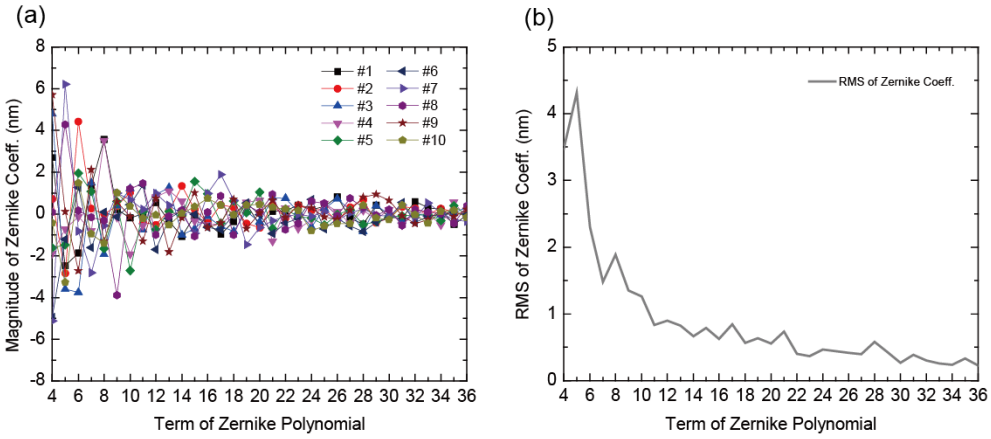

Fig. S4. Repeatability test of Shack-Hartmann surface metrology tool. (a) Ten measurements broken into 36 Zernike terms. In each measurement, the silicon wafer was mounted, measured, and removed from the wafer mount. (b) Calculated root-mean-square of the measured coefficients. The resulting profile was used as the noise floor in Figs. 4 and 7.

Five wafers patterned by gratings with different aspect ratios (Fig. 1(c))

To demonstrate the effect of grating lines trenched into silicon, we have patterned five silicon wafers (diameter 100 mm, thickness 0.525 mm, crystal orientation <100>) with fixed pitch (10 μm) and different aspect ratios (ARs from 0 to 1). The process is described as follows.

1. Six new silicon wafers were selected and their front side topography measured as initial profiles.
2. Wafers were piranha cleaned, followed by a dry oxidation process (1060 ℃, 4 hrs) to grow ~200 nm TOx on both sides as stressed coatings (approx. -70 N/m integrated stress).
3. The TOx layers were stripped from the front sides by using a buffered oxide etch (BOE). In this step, DOW SPR-700 photoresist (PR) was spin coated on the back sides to protect the stressed surfaces, and then removed by piranha after BOE.
4. Wafer front sides were measured with the TOx on the backside. By subtracting the initial profiles from Step 1, a spherical deformation is obtained, enabling calculation of the compressive stress in the TOx layers on each wafer based on the 3D FE model (6). In this step we assume the stresses in TOx layers are uniform.
5. 1 μm-thick PR (DOW SPR-700) layers were coated and baked on the wafer backsides for patterning purposes.
6. The PR-coated wafers were exposed by an MLA-150 patterning tool and developed in a developer solution (Microposit MF CD-26). Uniform grating lines with a fixed pitch of 10 μm were created in the PR horizontally (x direction). The PR pattern duty cycle (the width of the PR tooth divided by the pitch of the grating lines which is 10 μm) is ~70% due to limitations of the exposure tool.
7. The wafers with patterned PR gratings were hard baked (110 ℃, 1 hr) and then dipped in BOE for 3 min to remove the TOx within the unprotected areas. This isotropic wet etching does not impact the duty cycle since the TOx is much thinner than the width of the trench. The grating patterns have now been transferred into the 200 nm TOx layers.
8. The grating trenches were then etched into silicon by using a deep reactive ion etching (DRIE) tool. For each wafer the aspect ratio of the created grating teeth differs, varying from 0 to 1. This is achieved through control of the DRIE processing time. The first wafer has an AR zero since it was not processed through DRIE.
9. The wafers were cleaned in piranha solution to remove residual PR.
10. The wafers with back-side grating lines were measured by the S-H metrology tool. Deformations are calculated and plotted (Fig. S5) based on the initial profiles recorded in Step 1.

Based on the measured deformations, we used 3D finite element (FE) models to fit the profiles assuming the deformations are created by *fictitious stressed films* on the wafer backsides. Details of the 3D FE model fitting process are described in previous work (6). For the wafer with AR=0 (Fig. S5A), the stress is equibiaxial. The curvature of deformations before and after resist patterning/TOx etch are measured to calculate the area fraction of the remaining TOx which is determined by the width of the trenches in TOx layers. The area fraction is used to derive the equibiaxial stresses of each wafer (Step 4) before DRIE. For the wafers with AR from 0.05 to 1.05 (Figs. S5(b)-S5(f)), the deformations were fitted by astigmatism (Z_{22}) and sphere (Z_{20}) terms.

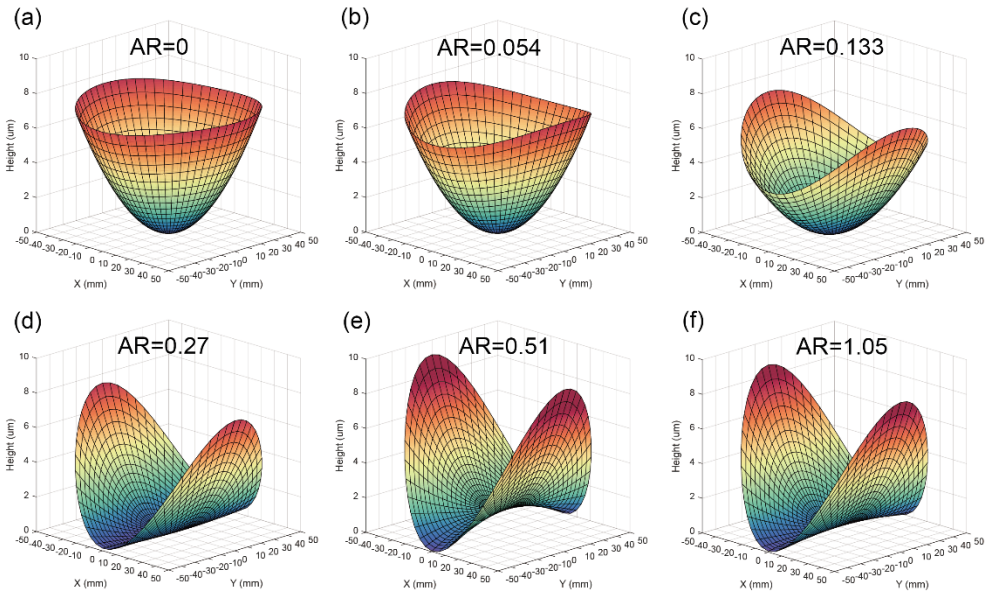

Fig. S5. Measured deformations generated by grating lines trenched into silicon with different aspect ratios. The pitch and the width of the lines are 10 μm and 3 μm, respectively. TOx on the back surface is 200 nm thick with no TOx on the front side. (a) Trenches are only in TOx layer, AR=0. (b) – (f) AR varies from 0.05 to 1.05.

The principal stresses along the y direction were calculated based on the FE models and then normalized by the derived equibiaxial stresses before DRIE. The results are depicted by the red squares in Fig. 1(c). The ratio of the curvatures between x and y directions are also calculated and plotted in Fig. 1(c) (blue circles). Note: a negative curvature along the y direction appears in Fig. S5(e), which is a direct illustration that tensile stress is imparted when AR=0.5.

Cylindrical pillars patterned on the backsides of silicon wafers

Grating trenches in silicon with AR=0.5 create a counterintuitive stress reversal as demonstrated by Figs. 1(c) and S5(e). However, a compressive uniaxial stress can generate a negative curvature along the perpendicular direction due to the Poisson's ratio of the substrate [7], which is indistinguishable from the effect of a tensile stress. The negative curvature in the y direction for AR=0.5 (Fig. S5(e)) is higher than that for AR=1 (Fig. S5(f)), which suggests an abnormal bending moment. In order to validate this prediction, we patterned cylindrical pillars trenched into silicon. Since the structure of cylindrical pillars is axially symmetric, the stress reversal due to the structure of AR=0.5 would appear equibiaxially. The equibiaxial stress-induced deformation (sphere) can be clearly observed and compared to the results derived from Stoney's equation. Figs. S6(a) and S6(b) clearly show that a toothed structure with a stressed top coating can generate stress reversal when AR=0.5. Although the cylindrical pillars are not in the same configuration as the one-dimensional grating trenches, these results directly demonstrate stress reversal induced by the tooth-structure when AR=0.5.

In addition, the solid blue line in Fig. 1(c) is a result of a classical model which assumes the trenches are only in the film. The AR in the classical model is defined as the height of the coating tooth versus the width. The classic model is derived from a two-dimensional Stoney's equation and assumes the trench gaps are comparable to the coating thickness [7]. The deviation between the blue circles and line in Fig. 1(c) demonstrates that the classic model cannot explain the stress reversal results.

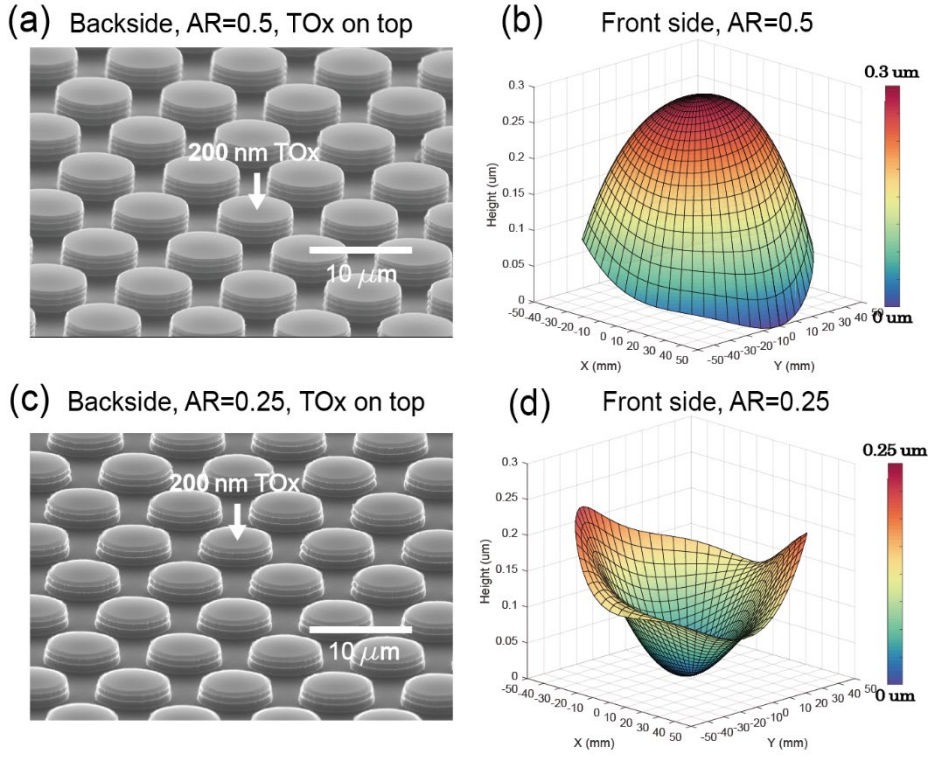

Fig. S6. Abnormal bending effect generated by high aspect ratio surface structures. Patterned structures of cylindrical pillars with TOx on the top create equibiaxial stress. (a) SEM image of a cylindrical pillar structure with AR=0.5, patterned on the backside of a silicon wafer. 200 nm of TOx is coated on the top of the pillars. (b) Measured deformation on the front side of the silicon wafer, demonstrating an equivalent tensile stress on the backside when AR=0.5. (c) and (d) Results for the case where AR=0.25.

Calibration of Type-I mesostructures

The Type-I mesostructure generates equibiaxial and uniaxial stresses simultaneously within each unit cell. Therefore, the trenched lines can lead to a relaxation of generated equibiaxial and uniaxial stresses, as depicted by Fig. S7, which can compromise stress control precision. Although Type-I provides the highest magnitude of stress among the three types, it requires a calibration process to connect the geometric parameters and the generated stresses. We define two parameters, 1) Duty Cycle (DC) and 2) Area Fraction (AF) (Fig. S7), which can be mapped to parameters A and B shown in Fig. 1(d). The DC represents the ratio of the area between the TOx disk and the unit circle (gray dashed line in Fig. S7). The AF is the area ratio between the grating-trenched area and the TOx disk. As a result, by controlling these two parameters, the magnitude of the uniaxial stress and equibiaxial stress can be manipulated. In order to achieve good precision, we performed the calibration process illustrated in Fig. S8.

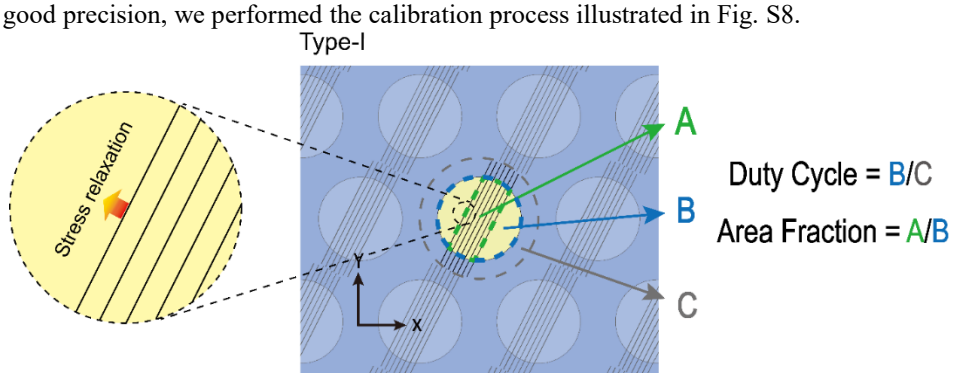

Fig. S7. Sketch of the Type-I mesostructure and its stress relaxation problem. Right: Region A represents the grating trenched area encircled by a dashed green line. Region B represents the TOx disk area enclosed by a dashed blue line. Region C indicates the unit circle area encircled by a dashed gray line. Left: Although the unpatterned TOx area is supposed to generate equibiaxial stress, the boundary of the trenched grating line can lead to a stress relaxation which influences the controlling precision.

We fabricated 20 wafers for testing different combinations of two-dimensional geometric parameters. Type-I mesostructured patterns with fixed DC, AF and grating rotation angle (horizontal) were uniformly patterned on the backside of each individual wafer. The DC and AF vary for different wafers from 0% to 100% for testing deformation creation. The topologies of the 20 wafers were monitored for comparison with calculated equibiaxial and uniaxial stresses based on the 3D FE model [6]. Fig. S8(a) shows microscope images of the unit cell regions from 16 wafers with different DCs and AFs. Fig. S8(b) depicts the corresponding measured deformations of those wafers. (The four samples with AF=0 were omitted since they only have equibiaxial stress and spherical deformations.) The 20 measured deformations were fitted by 3D FE models. The generated equibiaxial and uniaxial stresses are normalized by the value of equibiaxial stress when DC = 100% and AF = 0%. Results are plotted in Figs. S8(c) and S8(d) which are used as calibration maps. By using calibration map look-up tables, the model can determine the required DC and AF values to achieve target equibiaxial and uniaxial stresses and thus achieve desired deformations.

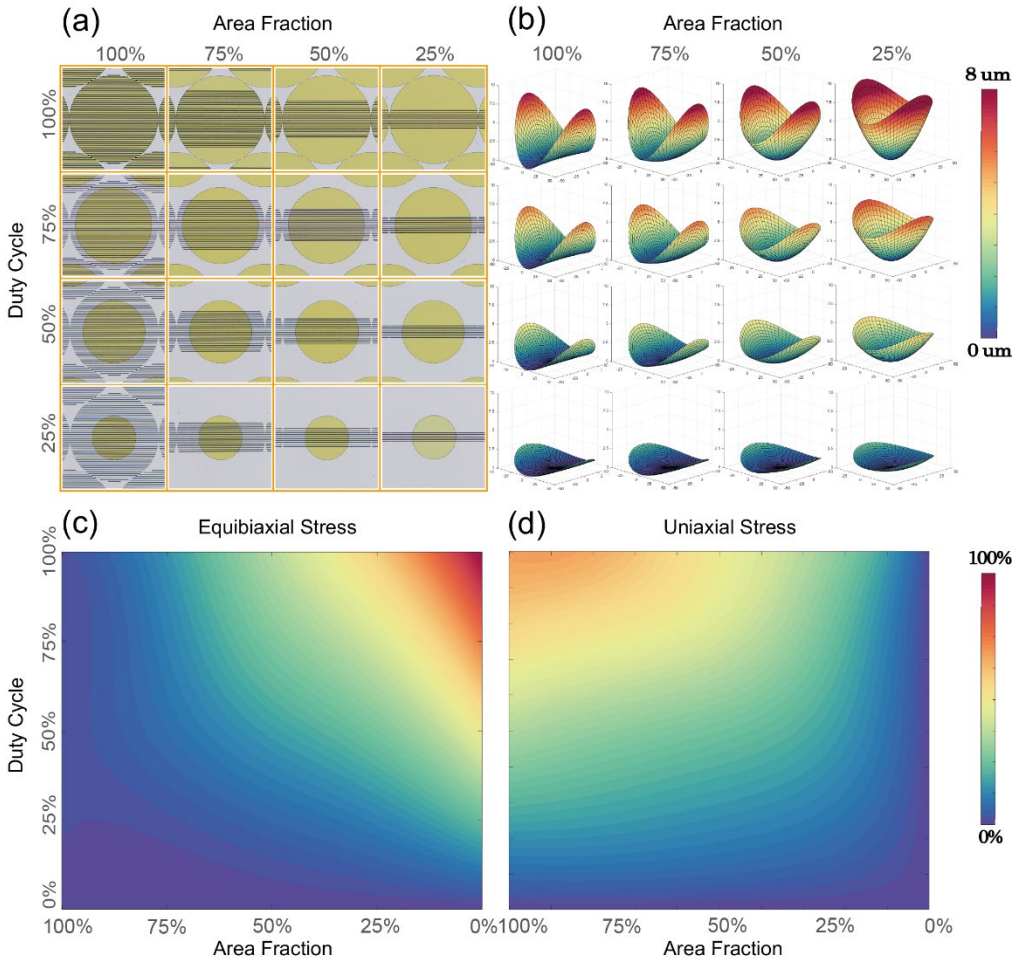

Fig. S8. Calibration of Type-I mesostructured patterns. (a) Microscope images of the unit cell regions on the backsides of 16 wafers. Each circle has different DC and AF values. (b) Measured deformations of silicon wafers generated by the patterns in (a). (c) and (d) Calibration maps of equibiaxial and uniaxial stresses for the two-dimensional variation of DC and AF. Note the maps were interpolated from 4 by 5 data points to 1000 by 1000 points.

The fabrication process for the 20 wafers is described as follows.

1. 20 new silicon wafers were selected and their front sides measured as initial profiles.
2. Wafers were piranha cleaned, followed by a dry oxidation process (1060 ℃, 4 hrs) to grow ~200 nm TOx on both sides as stressed coatings (approx. -70 N/m integrated stress).
3. The TOx layers were stripped from the front sides by using buffered oxide etch (BOE). In this step, SPR-700 photoresist (PR) was spin coated on the back sides and then removed by piranha after BOE to protect the stressed surfaces.
4. The topologies of the front sides were measured with the TOx on the backsides. By subtracting the initial profiles obtained from Step 1, spherical deformation is obtained, enabling calculation of the compressive stress in the TOx layers on each wafer. In this step we assume the stress is uniform in the TOx layers.

5. 1 μm thick PR (DOW SPR-700) layers were spin coated and baked on the backsides of wafers for patterning purposes.

6. The PR-coated wafers were exposed with an MLA-150 patterning tool, developed in Microposit MF CD-26, etched by BOE and then piranha cleaned. The TOx disks with the different DCs patterned on the backsides of 20 wafers were then ready for further processing. Note that at this stage no grating lines have yet been trenched into the TOx.

7. A patterned wafer was chosen with DC=100%. The deformation was measured and the equibiaxial stresses field was calculated assuming the patterned TOx is a fictitious uniform film.

8. The calculated equibiaxial stress is compared to the stress fields derived in Step 4. The stress on each wafer for normalization is therefore derived.

9. The wafers were again spin coated with SPR-700, patterned by the MLA-150 and then developed in CD-26 to create grating patterns in the PR, accurately aligned with the TOx disks.

10. The wafers with PR patterns were hard baked (110 ℃, 1 hr) and then dipped in BOE for 3 min to remove the TOx within the unprotected areas. The grating patterns have now been transferred to the 200 nm TOx layers.

11. The wafers with PR and TOx grating patterns are trenched into the silicon substrate using a deep reactive ion etching (DRIE) tool. For each wafer the aspect ratio of the created grating teeth is fixed (AR=1).

12. The wafers are piranha-cleaned to remove residual PR.

13. The wafers now with Type-I mesostructured patterns are measured by the S-H metrology tool. Deformations are generated and plotted (Fig. S8(b)) based on the differences with the initial profiles recorded in Step 1. The equibiaxial stresses and uniaxial stresses are calculated and then normalized by the stresses derived in Step 8.

14. The normalized stresses are interpolated to 1000 by 1000 data points and plotted in Figs. S8(c) and S8(d).

A solution for bimorph deformation with two stressed coating materials

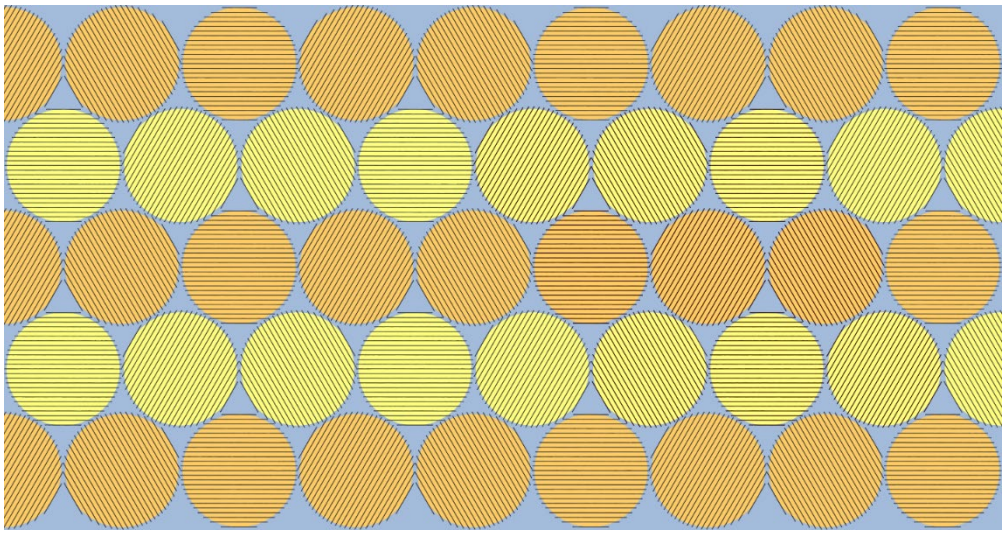

Fig. S9. Proposed Type-II mesostructure with two different stress providers. Orange regions represent coatings with tensile stress. Yellow represents compressive coatings.

A possible solution for bimorph deformation is to use two different stress providers on one substrate. For Type-I, the material of the stressed coating with each grating disk needs to be selected carefully. Fig. S9 shows a possible arrangement of two stressed coatings for the Type-II mesostructure. A candidate material for providing tensile stress could be a ceramic such as silicon nitride [8]. If the magnitude of the stress in each material is the same, the spatially averaged stress of the patterns depicted in Fig. S9 should be zero. We expect mesostructures such as the one in Fig. S9 could be integrated on the backside of new silicon wafers in the future, thus bi-directional topology control could be achieved after the front side is patterned with device and coating films.

Generation of trefoil by Type-I mesostructured (Figs. 2(a)-2(c))

In this demonstration, the backside stress provider is a TOx layer which intrinsically provides ~-300 MPa compressive stress. Since the generation of trefoil needs tensile stresses as demonstrated in Eq. 2, we decided to use a uniform TOx layer on the frontside to bias the shape. We assume the uniform compressive stress in the front side TOx is S_{front}, therefore the same compressive stress on the back side needs to be added in Eq. S2 to counteract the bias of the shape while generating the trefoil. When S_{front} is equal to $-S_0$, the stress field on the backside for generating the trefoil deformation is compressive everywhere, as demonstrated by Eq. S3.

$$N_1 = -S_0 \times (1 - \frac{r}{R}), \quad N_2 = -S_0 \times (1 + \frac{r}{R}), \quad \phi = \frac{1}{2}(\pi - \theta) \tag{S3}$$

The combination of two principal stresses in Eq. S3 can be translated to a combination of equibiaxial and uniaxial stresses, expressed as follows.

$$S_{equibiaxial} = -S_0 \times (1 - \frac{r}{R}), \quad S_{uniaxial} = -2S_0 \times \frac{r}{R}, \quad \phi = \frac{1}{2}(\pi - \theta) \tag{S4}$$

S_0 represents the maximum equibiaxial stress (when r=0 which is at the center of the wafer), and $2S_0$ stands for the maximum uniaxial stress (when r=R which is at the rim of the wafer).

The calibration maps of Fig. S8(c) and Fig. S8(d) shows that the maximum uniaxial stress is 66% of the magnitude of the equibiaxial stress when AF=1 and DC=1. Therefore, Eq. S4 is modified as,

$$S_{equibiaxial} = -0.33N_0 \times (1 - \frac{r}{R}), \quad S_{uniaxial} = -0.66N_0 \times \frac{r}{R}, \quad \phi = \frac{1}{2}(\pi - \theta) \tag{S5}$$

where N_0 is the equibiaxial stress when AF=0 and DC=1. Based on Eq. S5 and the calibration maps, the distributions of the DC, AF and the spin angle for the trefoil deformation can be determined to generate patterns for fabrication (Fig. 2(a)).

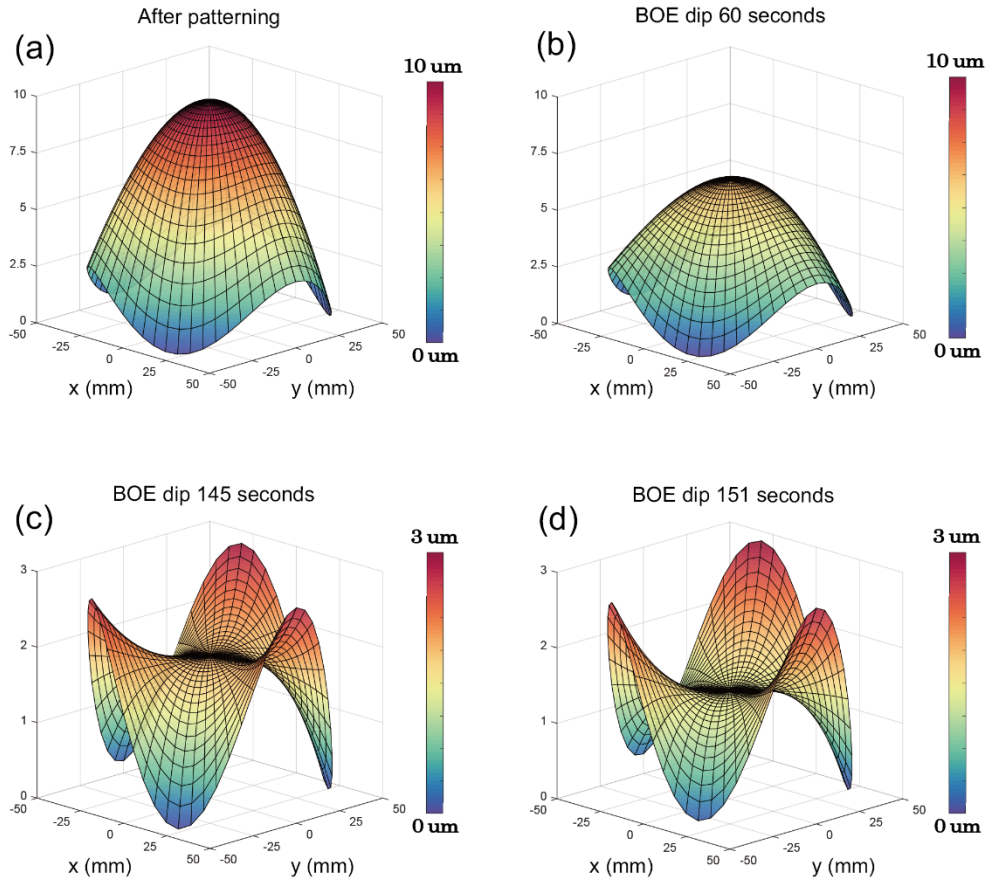

Fig. S10. Measured deformations of a patterned wafer when dipped in BOE for different times. In the process, the patterned side is protected by PR. (a) Deformation just after patterning the backside surface. (b) Deformation when dipped in BOE for 60 seconds. (d) After 145 seconds in total time, i.e., 85 seconds after (b). (d) 151 seconds total time.

The fabrication process is very similar to the one used for the calibration process, the only difference being the presence of a TOx layer on the front side. We preserve the front side TOx all through the steps until the last one – when the mesostructures are successfully patterned on the backside, and we perform an iteration process to uniformly reduce the thickness of the TOx layer on the front side until the measured spherical term (Z_{20}) reaches a minimum. Fig. S10 shows the evolution of the deformation when the TOx thickness on the front side is reduced. The iteration process for thinning the TOx film on the front side is described as follows.

1. The wafer's patterned side is spin coated by a thick layer of PR for protecting the trenched mesostructure.
2. The wafer is dipped in diluted BOE (1:3 - 1:10) so the TOx on the front side is etched uniformly and slowly. The etching time is controlled.
3. The wafer is piranha cleaned to strip the backside PR.
4. The deformation is measured. If the spherical term (Z_{20}) is not close to 0, recalculate the dipping time and repeat the process from Steps 1 to 4 until the profile is acceptable.

Shape correction with the Type-I mesostructure (Figs. 3(a)-3(c))

The tensor fields for producing deformations of the first 15 Zernike terms individually are listed in Table S1 (at the end of this supplemental material), which are derived from an analytical solution [1]. In order to flatten silicon wafers with initially curved profiles as shown in Fig. 3(a) (S-shape), the stress field, which is a linear combination of the tensors in Table S1, should be determined and patterned on the wafer backsides in accordance with the Zernike coefficients of the measured deformation. However, for these tests we used monocrystalline silicon wafers with <100> orientation where the Young's modulus of the material is orthotropic [9]. Therefore, the analytical solution based on substrates with isotropic material properties needs modification. In order to study the influence of the anisotropic properties, we established a FE model with the setting of orthotropic material. The model is a silicon wafer with a coating on the backside. The stress tensor field can be assigned to the coating for calculating the deformation. The Young's modulus of the silicon substrate is determined from a study [9]. By using the stress tensors in Table S1 derived for isotropic substrates, we attempt to generate the deformation of each Zernike term with the coefficient of 500 nm in the model. Results are shown in Table S2 (at the end of this supplemental material).

The modeling results show that some of the Zernike terms are influenced by the orthotropic substrate properties significantly. For example, for the Zernike term #13, which is 2nd order astigmatism $Z_{4\text{-}2}$, the generation of a 500 nm coefficient leads to 575 nm deformation of $Z_{4\text{-}2}$ and 889 nm deformation of $Z_{2\text{-}2}$ (astigmatism). Therefore, the correction based on the stress fields for isotropic substrates can result in low precision.

Our solution for this problem is expressed in Eq. S6. The FE modeling results are used as a matrix to achieve the target deformation.

$$\frac{1}{508}\cdot\begin{pmatrix} 508 & 0 & 0 & 6 & 1 & -1 & 0 & -248 & 13 & 0 & 155 & 0 \\ 0 & 791 & 0 & -2 & -14 & 0 & -3 & 0 & 0 & 889 & 0 & 6 \\ 0 & 0 & 509 & 17 & -3 & -3 & -1 & -44 & 57 & 0 & -5 & 0 \\ 0 & 0 & 0 & 543 & 0 & 36 & 0 & 8 & -6 & -1 & 1 & 0 \\ 0 & 0 & 0 & 0 & 548 & 0 & -35 & 1 & 1 & -6 & 0 & -2 \\ 0 & 0 & 0 & 108 & 0 & 629 & 0 & 36 & -30 & -2 & 4 & 1 \\ 0 & 0 & 0 & 0 & -122 & 0 & 626 & -7 & -5 & 12 & -1 & 3 \\ 0 & 0 & 0 & 1 & 0 & 0 & 0 & 564 & 1 & 0 & -41 & 0 \\ 0 & 0 & 0 & -1 & 0 & 0 & 0 & 4 & 506 & 0 & 0 & 0 \\ 0 & 0 & 0 & 0 & -2 & 0 & 0 & 0 & 0 & 575 & 0 & 1 \\ 0 & 0 & 0 & -7 & -1 & 1 & 0 & -148 & -15 & 0 & 635 & 0 \\ 0 & 0 & 0 & -1 & 4 & 0 & 1 & 0 & 0 & -6 & 0 & 618 \end{pmatrix}\begin{pmatrix} C_4 \\ C_5 \\ C_6 \\ C_7 \\ C_8 \\ C_9 \\ C_{10} \\ C_{11} \\ C_{12} \\ C_{13} \\ C_{14} \\ C_{15} \end{pmatrix} = \begin{pmatrix} 184.06 \\ 334.09 \\ 287.18 \\ -537.99 \\ -606.09 \\ -958.03 \\ 9.39 \\ -14.84 \\ 14.13 \\ -45.85 \\ 52.6 \\ -199.14 \end{pmatrix} \quad \text{(S6)}$$

Here $C_4 - C_{15}$ are the compensated Zernike coefficients derived from the measured deformation (S-shape in Fig. 3(a)) which is represented by the coefficients on the right side of the equation. By using compensated Zernike coefficients and the library of the stress tensors in Table S1, the tensor fields for flattening the profile of the silicon wafer are calculated and depicted in the following figure.

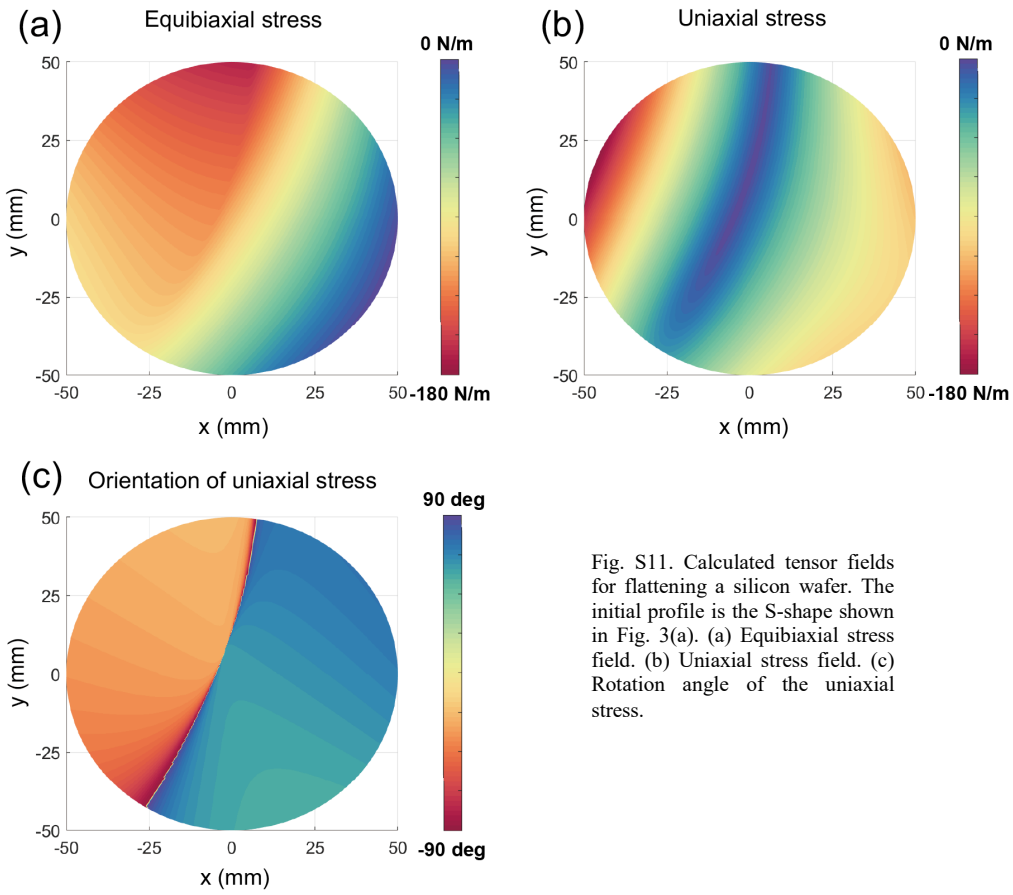

Fig. S11. Calculated tensor fields for flattening a silicon wafer. The initial profile is the S-shape shown in Fig. 3(a). (a) Equibiaxial stress field. (b) Uniaxial stress field. (c) Rotation angle of the uniaxial stress.

Based on this calculation, the required initial stress of the TOx layer on the backside before patterning was -464.8 N/m, corresponding to a thickness of 1.414 μm. The stress on the front side is -126.3 N/m which requires a 0.383 μm-thick TOx layer.

The calculated stress fields were converted to the maps of DC and AF by looking up the calibration maps in Fig. S8(c) and Fig. S8(d). Since the thicknesses of TOx layers on both sides need to be precisely controlled, we developed a strategy to achieve the required precision which is described as follows.

1. A wafer is selected and initial 2 μm-thick TOx layers are grown on both sides.
2. The wafer is dipped in BOE to reduce the thickness from 2 μm to 1.6 μm, slightly higher than the required thickness, so a stress margin is reserved for refined adjustments in the last steps.
3. The designed pattern is trenched into the backside. Since the thickness of the TOx is much larger than the ones we used for the calibration process and trefoil deformations, the patterning process is modified for better quality. A dry etcher (LAM-590) is used instead of BOE to trench the grating lines in the TOx layer.
4. After the patterning and cleaning processes, the surface profile of the deformed wafer is measured. At this stage, the spherical term (Z_{20}) should be under the correction target since the TOx on the front side is thicker than required. In the meantime, the remaining 11 Zernike terms ($Z_{2\text{-}2}$ to $Z_{4\text{-}4}$) are also over-corrected since the TOx on the

backside is thicker than needed, providing higher compressive stress leading to over-deformation.

5. The front side is spin coated with PR. The wafer is dipped in diluted BOE for a controlled period so the thicknes of the TOx layer on the backside is reduced.
6. The wafer is piranha cleaned and then measured by the metrology tool. The coefficients of the 11 Zernike terms should be close to zero.
7. If the flatness, excluding the spherical term, is not acceptable, then Steps 5 and 6 should be iteratively performed to achieve a good precision.

When the thickness of the TOx on the backside is satisfactory, we adjust the TOx on the front side in the same manner iteratively. When the spherical term Z_{20} is close to zero, the final flat topology is achieved as depicted in Fig. 3(a).

As a result, the RMS height of the silicon wafer was improved from 1.35 μm to 0.064 μm indicating an improvement factor of 21. The RMS slope error in the X direction was improved from 28 arcsecond to 0.862 arcsecond (32X) and in the Y direction from 16.9 arcsecond to 0.775 arcsecond (22X). The measured Zernike coefficients before and after correction are shown in Table S3.

Table S3. Measured Zernike coefficients before and after correction (nm).

	Z20	**Z2-2**	**Z22**	**Z3-1**	**Z31**	**Z3-3**
Before	184.06	334.09	287.18	-537.99	-606.09	-958.03
after	12.4	56.95	7.74	0.94	11.1	10.17
	Z33	**Z40**	**Z42**	**Z4-2**	**Z44**	**Z4-4**
Before	9.39	-14.84	14.13	-45.85	52.6	-199.1
after	-9.42	-4.26	3.19	5.23	14.02	10.15

The residual error is dominated by an astigmatism term (Z_{2-2}), which could be due to the inaccurate FE modeling of the orthotropic substrate. A calibration process for verifying the data in Table S2 could significantly improve the precision of the corrections.

Shape generation of trefoil and the secondary correction by Type-II mesostructure (Fig. 5(a)-(d))

The fabrication process for the Type-II mesostructure is similar to that for the calibration process (Fig. S8(a)). The following presents details of the pattern design.

$$\begin{bmatrix}\sigma_x\\ \sigma_y\\ \tau_{xy}\end{bmatrix}=\sum_{j=1}^{3}\begin{bmatrix}\cos^2(\theta_j) & \sin^2(\theta_j) & 2\cos(\theta_j)\sin(\theta_j)\\ \sin^2(\theta_j) & \cos^2(\theta_j) & -2\cos(\theta_j)\sin(\theta_j)\\ -\cos(\theta_j)\sin(\theta_j) & \cos(\theta_j)\sin(\theta_j) & \cos^2(\theta_j)-\sin^2(\theta_j)\end{bmatrix}\begin{bmatrix}\sigma_{uni,j}\\ 0\\ 0\end{bmatrix} \quad \text{(S7)}$$

The equation above shows the principal stresses in a unit cell for the type-II mesostructures. The $\sigma_{uni,1}$ represents the uniaxial stress with the orientation of θ_1 which is 0°. $\sigma_{uni,2}$ is the stress along 60°, and $\sigma_{uni,3}$ is along -60°. Based on the setting of the parameters, Eq. S7 can be written as

$$\begin{bmatrix}\sigma_x\\ \sigma_y\\ \tau_{xy}\end{bmatrix}=\begin{bmatrix}\sigma_{uni,1}+1/4\cdot(\sigma_{uni,2}+\sigma_{uni,3})\\ 3/4\cdot(\sigma_{uni,2}+\sigma_{uni,3})\\ \sqrt{3}/4\cdot(\sigma_{uni,3}-\sigma_{uni,2})\end{bmatrix} \quad \text{(S8)}$$

The stress field of trefoil can be expressed by

$$\begin{bmatrix}\sigma_x\\ \sigma_y\\ \tau_{xy}\end{bmatrix}=\begin{bmatrix}\cos^2(\phi) & \sin^2(\phi) & 2\cos(\phi)\sin(\phi)\\ \sin^2(\phi) & \cos^2(\phi) & -2\cos(\phi)\sin(\phi)\\ -\cos(\phi)\sin(\phi) & \cos(\phi)\sin(\phi) & \cos^2(\phi)-\sin^2(\phi)\end{bmatrix}\begin{bmatrix}\sigma\\ -\sigma\\ 0\end{bmatrix} \quad \text{(S9)}$$

$$\sigma=S_0\times\frac{r}{R},\ \phi=\frac{1}{2}(\pi-\theta)$$

where σ is the magnitude of the antibiaxial stress. The parameters S_0, r, R, ϕ and θ all have the same definition as in Eq. S2. By combining Eqs. S8 and S9, the uniaxial stresses required for generating the trefoil deformation, are expressed as follows.

$$\begin{bmatrix}\sigma_{uni,1}\\ \sigma_{uni,2}\\ \sigma_{uni,3}\end{bmatrix}=\begin{bmatrix}4/3\cdot S_0\cdot r/R\cdot(\cos^2(0.5\cdot(\pi-\theta))-\sin^2(0.5\cdot(\pi-\theta)))\\ 2/3\cdot S_0\cdot r/R\cdot(\sin^2(0.5\cdot(\pi-\theta))-\cos^2(0.5\cdot(\pi-\theta))+2\sqrt{3}\cos(0.5\cdot(\pi-\theta))\sin(0.5\cdot(\pi-\theta)))\\ 2/3\cdot S_0\cdot r/R\cdot(\sin^2(0.5\cdot(\pi-\theta))-\cos^2(0.5\cdot(\pi-\theta))-2\sqrt{3}\cos(0.5\cdot(\pi-\theta))\sin(0.5\cdot(\pi-\theta)))\end{bmatrix} \quad \text{(S10)}$$

In Eq. S10, the uniaxial stresses along the three directions need to be offset by a constant value to ensure compressive stress through the surface. The three offset stresses can be converted directly to the diameters of the TOx disks, as represented by C, D and E in Fig. 1(e). The parameter S_0 is optimized so the diameter of each TOx disk does not exceed 500 μm which is the boundary of the grating disks.

After the patterning process (Fig. 5(a)), the measured deformation (Fig. 5(b)) shows that one side lobe of the trefoil is slightly higher than the others, which is created by an unexpected astigmatism term (Z_{22}) depicted in Fig. 7. Since the Z_{22} can be corrected by a constant uniaxial stress in the x direction (Eq. S1), we decided to perform a secondary adjustment by patterning voids at the center of selected TOx disks which have the grating lines in the X direction. Since the stress to be removed is simple, we followed a strategy of secondary correction without calculation, described as follows.

1. Both sides of the patterned wafer were spin coated with PR (AZ5214).
2. The patterned surface was exposed by the MLA-150, developed, and BOE etched to create uniform voids in the TOx areas with grating lines in the X direction (Fig. 5(c)). In the first attempt, the void area was tiny for testing the secondary deformation (50 μm void's diameter).
3. The wafer is piranha cleaned and then measured for inspecting the Zernike coefficients.
4. If the suppression on Z_{22} is not satisfied, repeat the Steps 1 to 3 with larger voids patterning until the profile is acceptable.

Since the stress reduction on the backside may lead to an increase of the spherical term (Z_{20}), additional steps may be followed to reduce the thickness of the TOx on the front side. However, the reduction of equibiaxial stress is not the major goal of this demonstration and these steps were thus omitted.

We eventually performed four iterations of secondary correction. The void diameters were increased from 50 μm to 115 μm to achieve the results in Fig. 5(d). The Zernike coefficients for each iteration are listed in the following table.

Table S4. Measured Zernike coefficients for the iterations of secondary corrections (nm).

No.	**Z20**	**Z2-2**	**Z22**	**Z3-1**	**Z31**	**Z3-3**
1	97.19	9.46	44.58	2.36	16.14	12.82
2	107.33	11.58	34.30	1.90	11.76	16.43
3	88.97	5.33	15.26	12.48	17.52	10.66
4	93.92	13.13	2.97	5.22	13.92	15.06
No.	**Z33**	**Z40**	**Z42**	**Z4-2**	**Z44**	**Z4-4**
1	121.33	-7.71	0.55	-6.92	-1.69	5.41
2	127.30	-12.80	-2.12	-1.98	2.32	1.84
3	125.33	-11.32	2.47	-3.78	-2.65	6.22
4	125.09	-12.56	-1.38	-6.88	1.05	6.26

After four iterations, the target Zernike coefficient (Z_{22}) was successfully reduced from 44.58 nm to 2.97 nm, which successfully demonstrates the capability of secondary corrections on the Type-II mesostructure.

Shape generation of the trefoil by Type-III mesostructure (Figs. 6(a) and 6(b))

The design rule of the Type-III mesostructure is similar to the one of the Type-II. However, the fabrication process is different, which is described as follows:

1. A virgin silicon wafer is selected and frontside topology measured as the initial profile.
2. PR (SPR-700) is spin coated on the front side.
3. The wafer is exposed by the MLA-150 and then developed by developer (CD-26) to create grating lines in the PR.
4. The wafer was trenched by deep reactive ion etch (DRIE) to transfer the patterns from PR into the silicon surface. The aspect ratio (AR) was set to 1 for testing purposes. The trenched silicon surface is depicted in the background of Fig. 6(a).
5. The silicon wafers with grating line trenches are cleaned and thermally oxidized (1060 ℃, 3 hrs) to grow ~200 nm TOx on the surfaces including the sidewall and adjacent areas of the grating teeth.
6. The oxidized wafer is then spin coated with PR (AZ-5214) on both sides.
7. The trenched side is exposed by the MLA-150 and developed in AZ-422 to create PR disk patterns overlapping the grating circles.
8. The wafer is dipped in BOE and followed by a piranha cleaning to transfer the PR pattern into the TOx. The patterned surface at this stage is shown in the foreground of Fig. 6(a).

The wafer's front side was measured by our metrology tool for inspection. If the spherical term (Z_{20}) is not acceptable, an iteration process could be executed to reduce the thickness on the front side, which has been described in previous sections.

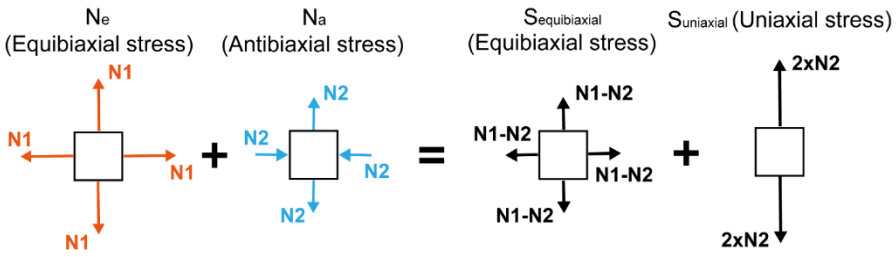

Fig. S12. Definition of N_e and N_a in Table S1.

Table S1. Stress fields for generating the deformation of each Zernike term with 100 nm RMS magnitude, derived from the analytical solution for isotropic substrates in ref. 30. N_e, N_a and N_s indicate equibiaxial stress, antibiaxial stress and shear stress represented by three Zernike polynomials. The explanation of N_e and N_a is shown in Fig. S12.

				Z_{20} (100 nm)				Z_{2-2} (100 nm)		
Noll	n	m		Ne (N/m)	Na (N/m)	Ns (N/m)		Ne (N/m)	Na (N/m)	Ns (N/m)
1	0	0		-2.325	0	0		0	0	-1.446
2	1	1		0	0	0		0	0	0
3	1	-1		0	0	0		0	0	0
4	2	0		0	0	0		0	0	0
5	2	-2		0	0	0		0	0	0
6	2	2		0	0	0		0	0	0
				Z_{22} (100 nm)				Z_{3-1} (100 nm)		
Noll	n	m		Ne (N/m)	Na (N/m)	Ns (N/m)		Ne (N/m)	Na (N/m)	Ns (N/m)
1	0	0		0	-1.446	0		0	0	0
2	1	1		0	0	0		0	0	-2.505
3	1	-1		0	0	0		-5.695	2.505	0
4	2	0		0	0	0		0	0	0
5	2	-2		0	0	0		0	0	0
6	2	2		0	0	0		0	0	0
				Z_{31} (100 nm)				Z_{3-3} (100 nm)		
Noll	n	m		Ne (N/m)	Na (N/m)	Ns (N/m)		Ne (N/m)	Na (N/m)	Ns (N/m)
1	0	0		0	0	0		0	0	0
2	1	1		-5.695	-2.505	0		0	0	-2.505
3	1	-1		0	0	-2.505		0	-2.505	0
4	2	0		0	0	0		0	0	0
5	2	-2		0	0	0		0	0	0
6	2	2		0	0	0		0	0	0
				Z_{33} (100 nm)				Z_{40} (100 nm)		
Noll	n	m		Ne (N/m)	Na (N/m)	Ns (N/m)		Ne (N/m)	Na (N/m)	Ns (N/m)
1	0	0		0	0	0		-9.004	0	0
2	1	1		0	-2.505	0		0	0	0
3	1	-1		0	0	2.505		0	0	0
4	2	0		0	0	0		-10.397	0	0
5	2	-2		0	0	0		0	0	-6.468
6	2	2		0	0	0		0	-6.468	0
				Z_{42} (100 nm)				Z_{4-2} (100 nm)		

Noll	n	m		Ne (N/m)	Na (N/m)	Ns (N/m)		Ne (N/m)	Na (N/m)	Ns (N/m)
1	0	0		0	-5.601	0		0	0	-5.601
2	1	1		0	0	0		0	0	0
3	1	-1		0	0	0		0	0	0
4	2	0		0	-6.468	0		0	0	-6.468
5	2	-2		0	0	0		-10.397	0	0
6	2	2		-10.397	0	0		0	0	0
				Z_{44} (100 nm)				**$Z_{4\text{-}4}$** (100 nm)		
Noll	n	m		Ne (N/m)	Na (N/m)	Ns (N/m)		Ne (N/m)	Na (N/m)	Ns (N/m)
1	0	0		0	0	0		0	0	0
2	1	1		0	0	0		0	0	0
3	1	-1		0	0	0		0	0	0
4	2	0		0	0	0		0	0	0
5	2	-2		0	0	4.573		0	-4.573	0
6	2	2		0	-4.573	0		0	0	-4.573

Table S2. FE modeling results when attempting to generate 500 nm RMS magnitude of each Zernike term on a <100> wafer (orthotropic material). The stress fields in Table S1 were used, which are derived for isotropic substrates.

	Target Zernike component (target: 500 nm RMS magnitude)											
Zernike component	**4** $Z_{2\text{-}0}$	**5** $Z_{2\text{-}2}$	**6** Z_{22}	**7** $Z_{3\text{-}1}$	**8** Z_{31}	**9** $Z_{3\text{-}3}$	**10** Z_{33}	**11** Z_{40}	**12** Z_{42}	**13** $Z_{4\text{-}2}$	**14** Z_{44}	**15** $Z_{4\text{-}4}$
4	508	0	0	6	1	-1	0	-248	13	0	155	0
5	0	791	0	-2	-14	0	-3	0	0	889	0	6
6	0	0	509	17	-3	-3	-1	-44	57	0	-5	0
7	0	0	0	543	0	36	0	8	-6	-1	1	0
8	0	0	0	0	548	0	-35	1	1	-6	0	-2
9	0	0	0	108	0	629	0	36	-30	-2	4	1
10	0	0	0	0	-122	0	626	-7	-5	12	-1	3
11	0	0	0	1	0	0	0	564	1	0	-41	0
12	0	0	0	-1	0	0	0	4	506	0	0	0
13	0	0	0	0	-2	0	0	0	0	575	0	1
14	0	0	0	-7	-1	1	0	-148	-15	0	635	0
15	0	0	0	-1	4	0	1	0	0	-6	0	618

References

1. B. D. Chalifoux, R. K. Heilmann, and M. L. Schattenburg, "Correcting flat mirrors with surface stress: analytical stress fields," JOSA **35**, 1705-1716 (2018).
2. Y. Yao, B. Chalifoux, R. K. Heilmann, and M. L. Schattenburg, "Thermal oxide patterning method for compensating coating stress in silicon substrates," Opt. Express **27**, 1010-1024 (2019).
3. Y. Yao, X. Wang, J. Cao, and M. P. Ulmer, "Stress manipulated coating for fabricating lightweight x-ray telescope mirrors," Opt. Express **23**, 28605-28618 (2015).
4. C. Forest, C. Canizares, D. Neal, M. McGuirk, A. Slocum, and M. L. Schattenburg, "Metrology of thin transparent optics using Shack-Hartmann wavcfront sensing," Opt. Eng. **43**, 742-753 (2004).
5. M. Akilian, C. Forest, A. Slocum, D. Trumper, and M. L. Schattenburg, "Thin optic constraint," Precis. Eng. **31**, 130-138 (2006).
6. B. D. Chalifoux, E. Sung, R. K. Heilmann, and M. L. Schattenburg, "High-precision figure correction of x-ray telescope optics using ion implantation," Proc. SPIE **8861**, 88610T (2013).
7. Freund, and S. Sursesh, "Thin film materials: stress, defect formation and surface evolution" Cambridge Univ. Press, Page 205 (2003).
8. M. Martyniuk, J. Antoszewski, C. A. Musca, J. M. Dell, and L. Faraone, "Stress in low-temperature plasma enhanced chemical vapour deposited silicon nitride thin films," Smart Mater. Struct. **15**, S29-S38 (2005).
9. M. A. Hopcroft, W. D. Nix, and T. W. Kenny, "What is the Young's modulus of silicon?," J. Microelectromech. Syst. **19**, 229-238 (2010).